Enhanced UV-C Detection of Perovskite Photodetector Arrays via Inorganic $CsPbBr_3$ Quantum Dot Down-Conversion Layer

*Taoyu Zou, Xiyuan Liu, Renzheng Qiu, Ya Wang, Shuyi Huang, Chuan Liu, Qing Dai, and Hang Zhou**

Organometal halide perovskites have been considered as promising candidates for high-performance low-cost photodetectors. Nonetheless, as perovskite photodetectors are usually built on glass or polymer substrates, their UV-C (200–280 nm) photodetection ability is quite limited due to the high absorption of glass or polymer substrates. Here, a uniform UV photodetector array which integrates perovskite photodiodes with inorganic $CsPbBr_3$ quantum dot (QD) fluorophor is reported. $CsPbBr_3$ quantum dot fluorophor not only acts as an efficient down-conversion layer to convert UV light into 510 nm light, but also functions as a protective layer to prevent degradation of hybrid organic–inorganic perovskite by UV light. Compared to direct UV-C (279 nm) detection with perovskite photodiode, the QD integrated photodetector shows a higher responsibility and detectivity to UV-C, with values enhanced by 1 order in magnitude. This work provides a low-cost and effective approach for all perovskite-based UV-C photodetectors and imagers.

Hybrid organic–inorganic perovskite materials, such as $CH_3NH_3PbI_3$, have attracted broad attention due to their excellent optoelectronic properties, such as high light absorption coefficient, long charge carrier lifetime and diffusion length, and tunable bandgap.[1] They have been widely adopted as the light absorbing layer in different types of photodetectors to convert light signals into electrical signals.[2] Perovskite photodiode presents the advantages of low dark current, fast response speed, and high detectivity.[1b,3] They have also been applied to detect light ranging from X-ray,[4] UV,[5] to near-infrared (NIR) wavelengths.[6]

The detection of UV light presents a wide range of applications, such as chemical, health, infrastructure, environment and biological analysis and monitoring, flame detection, unattended stations, astronomical studies, optical communications, and emitter calibration.[7] There are several reports on perovskite UV photo-diodes for detection of UV-A (400–320 nm) light.[5b,8] However, reports of perovskite photodiode for the detection of UV-C (280–200 nm) light is rarely reported. UV-C detection and imaging are very important for DUV lithography stepper,[9] surface contamination inspection, and for UV astronomy.[10] Conventional standard silicon charge-coupled devices (CCDs)/complementary metal oxide semiconductor (CMOS) camera is less sensitive to deep UV light, due to the extremely short absorption depth, i.e., 5 nm at 250 nm wavelength. Therefore, there is a growing demand for developing new types of DUV detectors or cameras for imaging applications. The difficulties of UV-C detection can be ascribed to two reasons. First, perovskite-based photodiodes are normally fabricated on transparent conducting oxide (TCO) glass that absorbs most of the UV photons below 350 nm, leading to relatively low photogenerated carriers in the perovskite layer. Second, a long-term exposure under the UV light could cause significant degradation of the perovskite-based photodiode.[11] In this regard, it remains a challenge to rationally design high-performance perovskite-based photodiode for the detection to spectral regions including UV-C (280–200 nm), and even far UV (200–10 nm).

All inorganic cesium lead halide perovskites ($CsPbX_3$, X = Cl, Br, or I) nanocrystals or quantum dots possess outstanding optical properties such as high photoluminescence quantum yields, narrow line width, and short radiative lifetime, which make them a promising material for practical optoelectronic applications.[12] Particularly, the ability to convert high energy of photons into low-energy visible photons by direct bandgap emissions allows $CsPbX_3$ QDs to be a promising fluorophor material in X-ray detection.[12c,13] For example, Chen et al. determined the intense radioluminescence of all inorganic

T. Zou, X. Liu, R. Qiu, Y. Wang, Prof. H. Zhou
School of Electronic and Computer Engineering
Peking University Shenzhen Graduate School
Shenzhen 518055, P. R. China
E-mail: zhouh81@pkusz.edu.cn

S. Huang
Key Lab of Advanced Micro/Nano Electronic Devices & Smart Systems of Zhejiang
College of Information Science and Electronic Engineering
Zhejiang University
Hangzhou 310027, P. R. China

Prof. C. Liu
State Key Laboratory of Optoelectronic Materials and Technologies
School of Electronics and Information Technology
Sun Yat-Sen University
Guangzhou 510006, P. R. China

Prof. Q. Dai
National Center for Nanoscience & Technology
Beijing 100190, P. R. China

$CsPbX_3$ perovskite nanocrystal fluorophor to X-ray with a photoluminescence quantum yield (PLQY) of 58.6%, and reported the application for X-ray imaging for the first time.[12c] Lu et al. reported a $CsPbX_3$ QDs silicon nanowires radial junction structure for ultrafast and highly sensitive solar-blind UV detection, in which UV light is down converted into longer wavelengths at ≈510 nm by $CsPbX_3$ QDs, and also revealed the air-exposure stability of the Si-based $CsPbX_3$ QDs UV detectors in their case.[14] In addition to the integration of the all inorganic perovskite quantum dots, Zhang et al. explored the integration of hybrid organic–inorganic $MAPbBr_3$ quantum dots with silicon photodetector toward broadband and solar-blind light detection, in which $MAPbBr_3$ quantum dots show a good photostability under a long-term 365 nm irradiation.[15] By modulating the anionic component and quantum dot size, the photoluminescence emission spectra of $CsPbX_3$ QDs can also be tuned across the visible spectrum,[12b] which perfectly match the absorption spectrum of most hybrid organic–inorganic perovskite materials. So far, there is no report on the integration of perovskite-based photodiode with $CsPbX_3$ QDs fluorophor for UV light detection. In an attempt of combining the merits of $CsPbX_3$ QDs and hybrid organic–inorganic perovskite materials, here, we propose a highly sensitive UV photodetector array consisting of a perovskite-based photodiode and $CsPbX_3$ QDs UV down-conversion layer for improved UV-C detection.

The transmission electron microscope (TEM) image in **Figure 1**a demonstrates a cubic shape of as-synthesized $CsPbBr_3$ QDs, with an edge length of ≈20 nm. The crystal structure for our as-prepared $CsPbBr_3$ QDs is certified by X-ray diffraction (XRD) in Figure 1b. The XRD pattern of the $CsPbBr_3$ QDs is in accordance with the simulated XRD pattern based on the crystallographic information framework (CIF) file, which reveals that our as-prepared $CsPbBr_3$ QDs have a cubic phase. To obtain the fluorescence property, the emission and excitation spectra of the $CsPbBr_3$ quantum dots were examined by the steady-state photoluminescence (PL) shown in Figure 1c. When under 275 nm UV light excitation, the $CsPbBr_3$ QDs exhibit a narrow emission spectrum with a peak at 510 nm and a full width at half maximum (FWHM) of about 33 nm. It is worth to note that the PL excitation spectrum of these $CsPbBr_3$ quantum dots cover the entire UV spectral region, which means $CsPbBr_3$ quantum dots could efficiently down convert UV light ranging from UV-A to UV-C into ≈510 nm light. The absolute photoluminescence quantum yield (PLQY) of the $CsPbBr_3$ QD solution used in our work is 39.5%. As shown in the inset of Figure 1c, our as-prepared $CsPbBr_3$ QDs solution in cyclohexane shows bright green color, when illuminated by UV light.

We then investigate the photon conversion relationship between UV light and the down-converted 510 nm light with a setup illustrated in Figure 1d. UV light emitting diodes (LEDs) (SMD 3030 and 6363, 275 nm) were used as the radiation source, and the spectra of which were calibrated with corresponding peaks located at 279 nm (Figure S1a, Supporting Information). The intensity of the UV light was controlled by a DC power. The fluorophor film

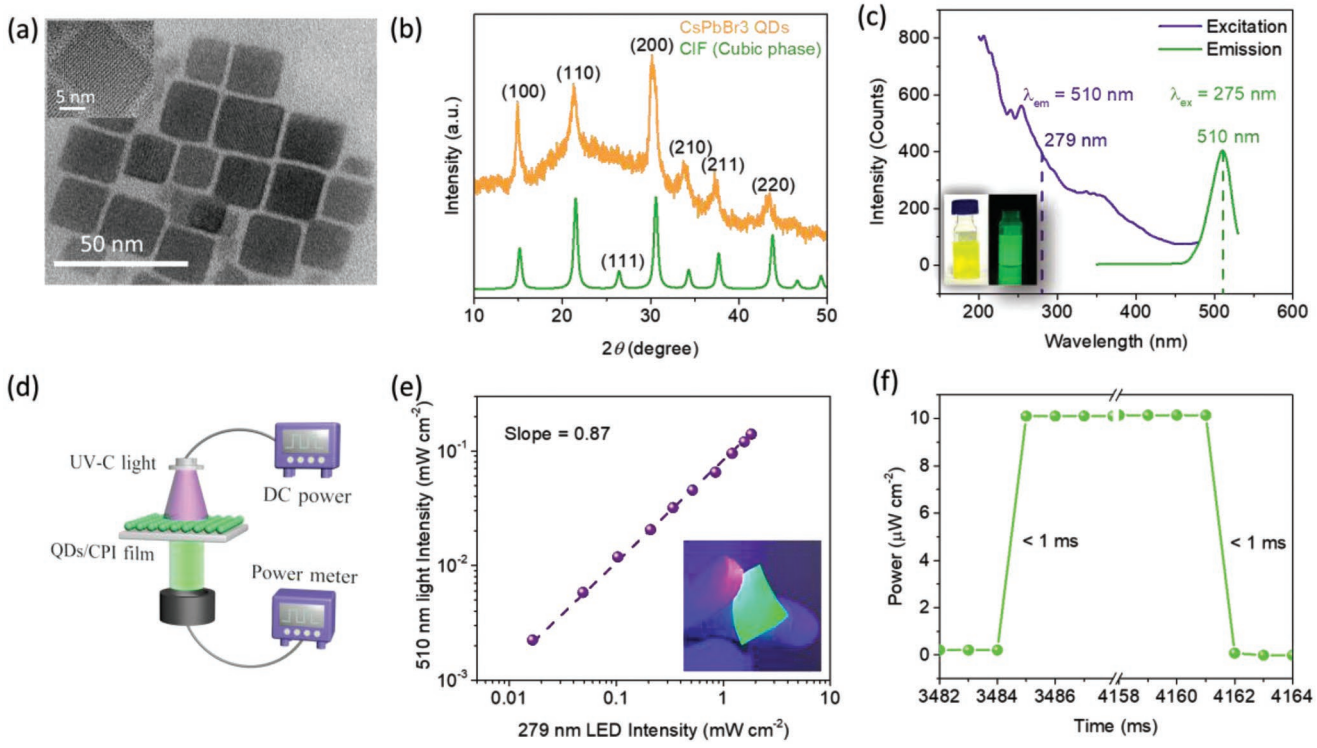

Figure 1. a) High-resolution TEM images of $CsPbBr_3$ quantum dots. b) XRD patterns for as-grown $CsPbBr_3$ quantum dots as well as the simulation based on the cubic phase CIF file. c) PL emission and excitation spectra of the $CsPbBr_3$ quantum dots and the inset shows the photo of as-prepared $CsPbBr_3$ QDs solution in cyclohexane under white light or UV light illumination. d) Schematic illustration of the experimental setup for quantum dot thin film UV down-conversion light intensity measurement. e) Plots of converted light intensity (510 nm) versus incident light intensity; inset shows the photograph of $CsPbBr_3$ quantum dot fluorophor under UV light excitation. f) Photoresponse of $CsPbBr_3$ quantum dots fluorophor to incident 279 nm light.

was made by casting $CsPbBr_3$ QDs onto a colorless polyimide (CPI) film. An optical power meter (Newport, 1936-R) is placed under the CPI film to measure the light intensity of the down-converted 510 nm light. Figure S2 in the Supporting Information reveals the influence of QDs film thickness on the light intensity of converted 510 nm light. Figure 1e shows the photograph of $CsPbBr_3$ quantum dot fluorophor when illuminated by UV light. The thickness of deposited $CsPbBr_3$ quantum dot thin film is ≈1 μm which is measured by the Stylus Profilers. The dependence of the converted 510 nm light intensity on the incident 279 nm light intensity ranging from 0.017 to 1.827 mW cm^{-2} is investigated as shown in Figure 1e. For the 1 mW cm^{-2} 279 nm light, after passing through the CPI film, the intensity decreases to 0.015 mW cm^{-2} (Figure S1b, Supporting Information), which is almost 2 orders magnitude smaller. Upon 279 nm UV light illumination, the intensity of converted 510 nm light is nearly 1 order in magnitude lower, ranging from 0.002 to 0.140 mW cm^{-2}, probably due to the light transmission losses when passing through the CPI film and the photon loss due to the light scattering. It is important that the downshifted 510 nm light intensity is linearly proportional to the radiated UV light intensity in our measurement ranges with a slope of 0.87. Although the down-converted 510 nm light is weaker than the incident 279 nm light, the perovskite photodiode integrated with $CsPbBr_3$ QDs fluorophor shows a better performance to 279 nm light detection, compared to the direct detection device, which will be described below.

Further, the photoresponse repeatability and speed of the fluorophor film are illustrated in Figure 1f and Figure S3 (Supporting Information). The rise or decay time are usually defined as the required time for the photointensity transition from 10% to 90% or from 90% to 10% of the steady-state photon intensity. Herein, the rise or decay time was measured as short as <1 ms. It is worth noting that the radiative recombination lifetimes of $CsPbX_3$ QDs are quite short (usually in the range of nanoseconds).[16] The fast response and recovery speeds for the photo-to-photo conversion characteristics meet the photodetection in most applications.

The fabrication of photodiode array is one of key steps toward image sensing application. Although previously perovskite photodiode array has been fabricated through flash-evaporation printing methodology,[17] spin-on-patterning (SoP) process,[18] and vapor–solid–solid reaction (VSSR) process,[19] the uniformity of the electrical performance of each device in the array is far from ideal. One of the main reasons that lead to nonuniformity of the perovskite device is the incomplete reaction of PbI_2 with methyl ammonium iodide (MAI), which causes PbI_2 to remain in the perovskite layer. To tackle this problem, we sequentially deposited MAI/PbI_2/MAI layers for realizing 10 × 10 perovskite photodiode arrays with high uniformity of electrical performance. The fabrication procedure is briefly described as following in **Figure 2**a. First, MAI thin film was spin coated on the patterned indium tin oxide (ITO) glass. Then, PbI_2 powders were thermally evaporated on the bottom MAI layer via a fine metal mask, while, for the control sample, PbI_2 powders were directly deposited on the ITO glass. After spin coating the MAI thin film onto the PbI_2 thin film, the substrate was annealed for the fully crystallized perovskite layer. To complete the photodiode, other functional layers, such as an electron transport layer and the metal electrode, were sequentially deposited on the top of the perovskite layers. The image of a 10 × 10 photodiode arrays is present in Figure 2b.

The dark- and photo-current signals of each single pixel in the 10 × 10 photodiode arrays are presented in Figure 2c. It can be seen that all the photodiodes in the array can function with a dark current median value of 7.40×10^{-7} mA when biased at −0.1 V. The low dark current is beneficial for the detection of weak light. The on/off ratio was further extracted, as shown in Figure 2d, with a high median ratio of 8.16×10^4. The corresponding dark and light current mapping is shown in Figure 2e,f. There is only one pixel is found to be malfunctioned out of 100 pixels, demonstrating the excellent reproducibility of each pixel within the photodiode array. The median value of photocurrent for all tested pixels is 6.23×10^{-2} mA with a small fluctuation ($\pm 1.53 \times 10^{-2}$ mA), indicating a high photoresponse uniformity. In contrast, for the device without MAI bottom layer, the sensor array shows a large fluctuation in the dark and photocurrent, and a low yield of pixels, as shown in Figure S4 in the Supporting Information. The dark currents for a device without MAI as the seed layer range from 7.0×10^{-8} to 8.4×10^{-4} mA, and meanwhile, there are 3 pixels is defective within 10 pixels in the diagonal line, which, to a great extent, will reduce the recognition to images. Therefore, we provide an approach, with MAI as a seed layer, to induce the formation of perovskite thin film toward a high uniformity of photodiode array.

The *J*–*V* curve of one of the typical photodiodes is shown in Figure S5a in the Supporting Information under the illumination by monochromatic light of 520 nm with the light intensity ranging from 0.035 to 1.180 mW cm^{-2}. The dependency of current density (*J*) to incident light for three randomly chosen pixels from the array is also present in Figure S5b in the Supporting Information. Notably, these three photodiodes possess similar photocurrent at a different light intensity, which further proves the reproducibility of photodiodes in the array. It should be pointed out that the photocurrent shows a linear dependence on the incident light intensity, which can be quantitatively described by linear dynamic range (LDR) as shown in Figure S5c in the Supporting Information. The LDR, expressed by 20 log (J_{ph}/J_d), where J_{ph} and J_d are photo- and dark-current density, is estimated to be 83.7 dB at a light intensity of 1 mW cm^{-2} at −0.1 V, which is higher than that of InGaAs photodetector (66 dB).[20]

Furthermore, the responsivity *R* and the specific detectivity *D** of a perovskite photodetector is evaluated. R can be calculated by $(J_{ph}-J_d)/P$, where *P* is the light intensity. The specific detectivity *D** can be obtained by $(AB)^{1/2}$/NEP, where *A* is the device area, and *B* is the bandwidth. NEP is the noise equivalent power, which is defined as i_n/R, where i_n is the measured total noise. The total noise is generally dominated by shot noise and thermal noise in perovskite photodetector.[3b,21] If the shot noise is the main contribution to the dark current, then, the *D** can be calculated by $R\ (2\ q\ J_d)^{-1/2}$, where *q* is the and elementary charge.[3b,21] Here, we estimated the *D** for reference by assuming the shot noise is the dominant noise. The value of *D** to different incident light intensity is plotted in Figure S4d in the Supporting Information under 520 nm light illumination at −0.1 V bias voltage. The *D** is calculated to be ≈1×10^{12} Jones, which is comparable to that of commercial InGaAs and silicon-based photodetector (≈10^{11}–10^{12} Jones),[22] indicating the potential for the practical application of our photodiode array.

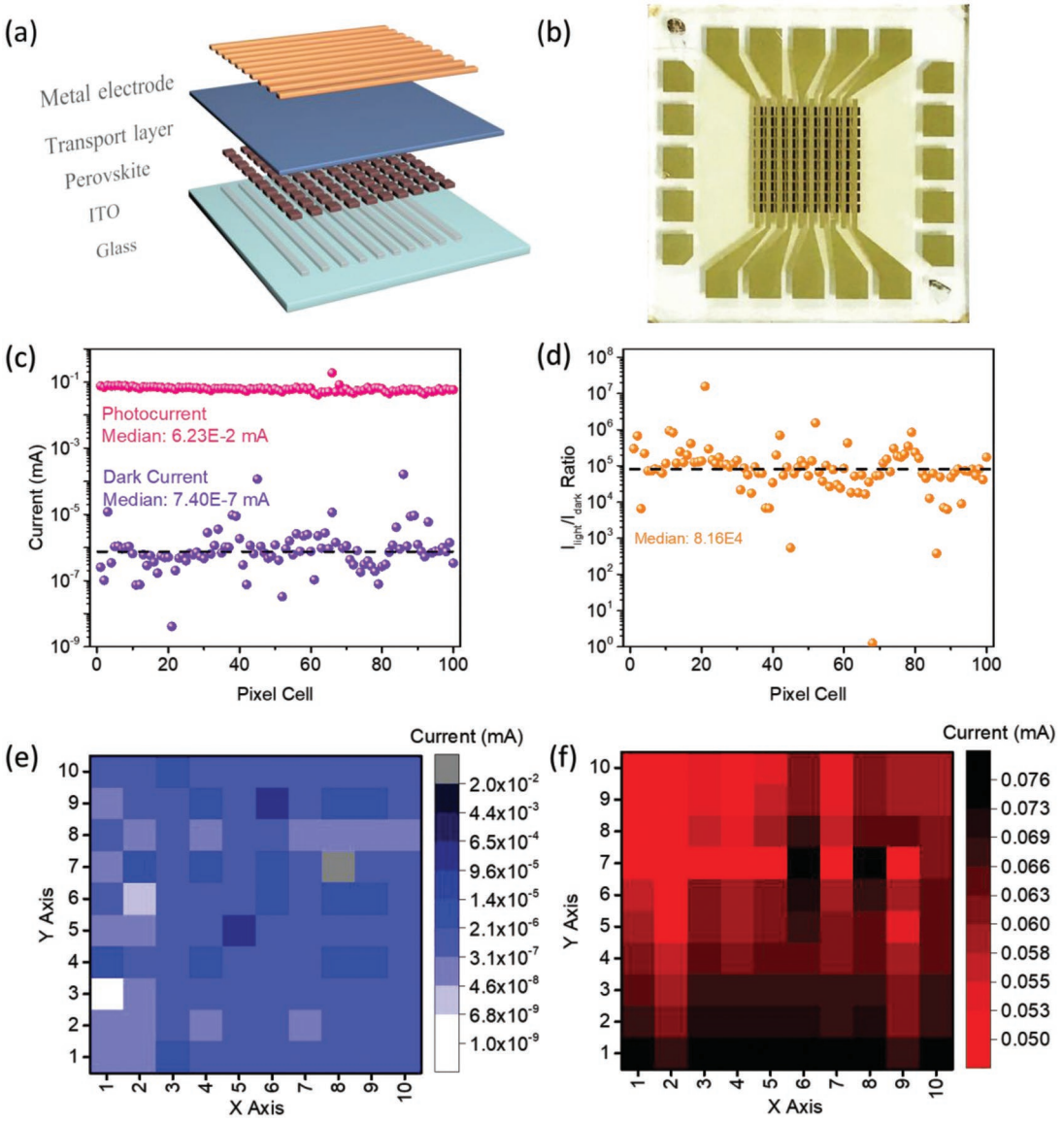

Figure 2. a) Schematic and b) optical image of the $MAPbI_3$ perovskite photodiode array. The physical size of the as-prepared photodetector is 3 cm × 3 cm. The width for ITO and Au electrode in a pixel is 500 and 500 µm, respectively, with the effective area in one photodiode pixel of ≈0.25 mm^2. The size for one perovskite pixel is 800 µm × 800 µm. c) Dark current and the corresponding photocurrent for each pixel under −0.1 V and the calculated median value for dark current and photocurrent, respectively. d) Extracted on/off ratio for each pixel. e,f) Dark and photocurrent mapping of the 10 × 10 perovskite-based photodiode array under a white light illumination biased at −0.1 V.

Figure S6a in the Supporting Information shows the transient photocurrent response to an incident LED light (520 nm, 404.7 µW cm^{-2}) at −0.1 V. The LED light is controlled by a function generator for an interval light signal. The result manifests a fast photoresponse of the photodiode to incident light with a rise time of <48 ms and a fall time of <46 ms, which is limited by our measurement equipment, and with a stable and repeatable on/off ratio of 3.71×10^3, which demonstrate the rapid separation of the photogenerated electrons and holes and the effective collection by corresponding electrodes. It should be mentioned that the temporal resolution of the human eye is about 25 Hz (40 ms).[23] Besides, after thousands of cycles on/off operation (Figure S6b, Supporting Information), there is almost no difference in the dark and photocurrent, respectively, implying the excellent repeatability and reliability of our photodiode.

We further confirmed the feasibility of our proposed concept by integrating perovskite photodiode with $CsPbBr_3$ QDs fluorophor to extend and improve the detection to UV-C light. **Figure 3**a shows the schematic diagram of the integrated UV light photodetector, which is made up a perovskite-based photodiode and $CsPbBr_3$ QDs fluorophor. Figure 3b shows the successful detection of our photodetection system to 279 nm light. Once under the illumination of 279 nm light, the photodetection system shows a fast response and reaches a steady state, with a rise time of <70 ms. When the light is turned off, the

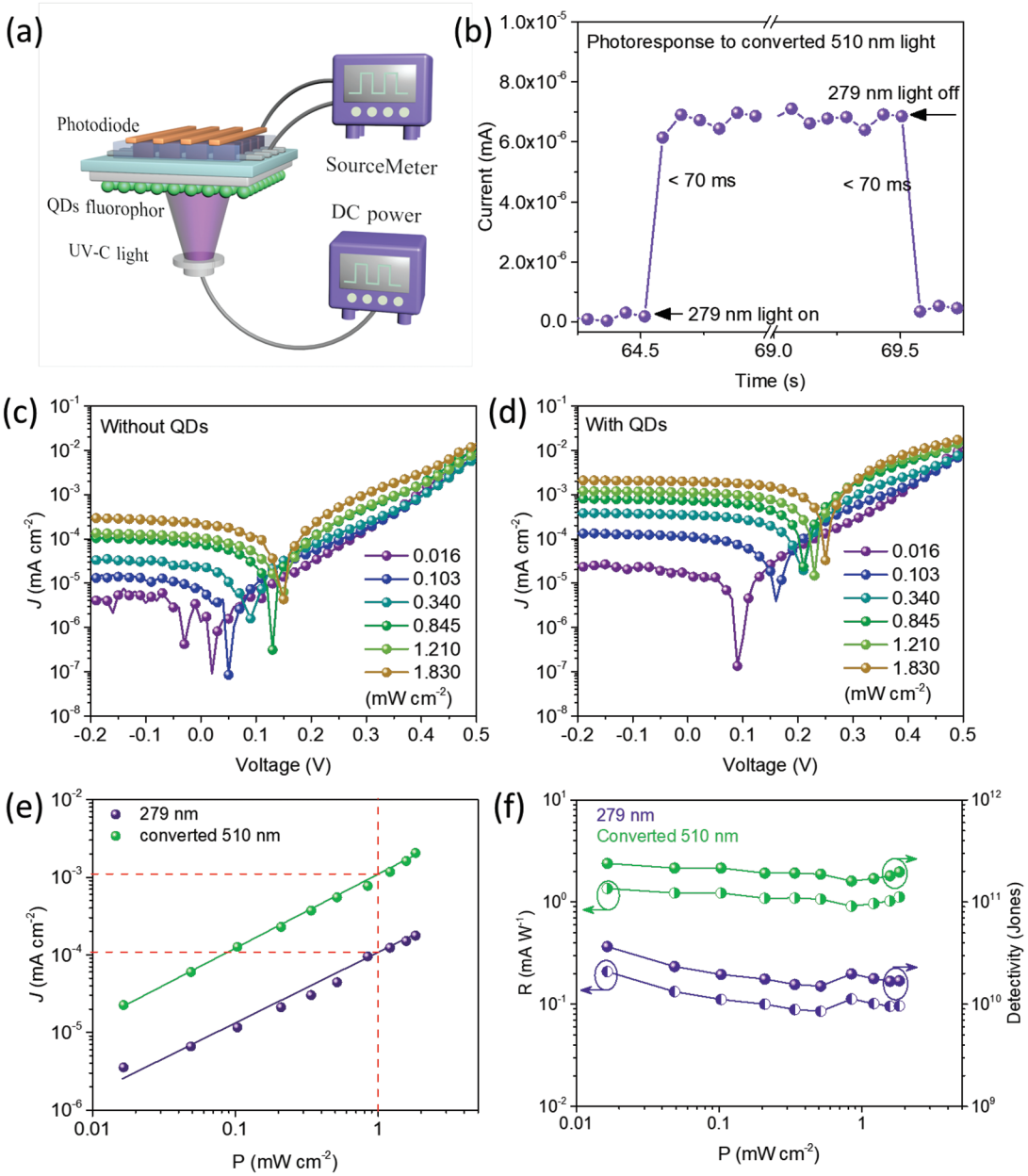

Figure 3. a) Schematic diagram of integrated photodetection system comprising photodiode arrays and $CsPbBr_3$ QD fluorophor. b) Transient photocurrent response of our photodetection system to 279 nm UV-C light. c,d) Measured *J–V* curve of the photodiode with and without $CsPbBr_3$ QDs fluorophor under 279 nm illumination. e) Photocurrent values of the photodiode to the 279 nm light with different light intensity and to correspondingly converted 510 nm light by $CsPbBr_3$ QDs fluorophore at –0.1 V. f) Responsibility and detectivity of the photodiode to 279 nm UV-C light and accordingly converted 510 nm light by $CsPbBr_3$ QDs fluorophore at –0.1 V.

photocurrent quickly decreases with a decay time of <70 ms. In order to gain more insights into the performance of our UV photodetection system, we investigated the photoresponse characteristics to 279 nm UV wavelength and light intensity ranging from μW cm^{-2} to mW cm^{-2}. The photocurrent value at –0.1 V for 279 nm and converted 510 nm light are drawn in Figure 3e (The full *J–V* curve is shown in Figure 3c,d). The log–log plot of the photocurrent exhibits good linearity with light intensity to both 279 nm and down-converted 510 nm light. It is obvious that the photocurrent is about 1 order magnitude larger when the incident 279 nm light is converted into 510 nm light. Accordingly, the responsivity (*R*) and detectivity (*D**) for photodetector with or without $CsPbBr_3$ QDs fluorophor were evaluated and plotted in Figure 3f. It is not surprising that the integrated photodetection system with $CsPbBr_3$ QDs as fluorophor shows much better performance, with a maximum *R* and *D** value of ≈1.4 mA W^{-1} and ≈2.4×10^{11} Jones, respectively. The detectivity in our case is much higher than that of previously reported $CH_3NH_3PbCl_3$ perovskite-based UV-A photodiode and even higher than that of $CH_3NH_3PbCl_3$ single

crystals photodetector and $CH_3NH_3PbI_3$ thin film-based UV-A photoconductor. For comparison, when directly detecting the UV-C (279 nm) light, the R and D* value shows a relatively low R and D^* value of 0.2 mA W^{-1} and 3.7×10^{10} Jones, respectively. Moreover, in the photodiode, the open-circuit voltage (V_{oc}) can be expressed as (n k T/q) ln (J_{ph}/J_s + 1),[24] where n, k, and T are ideality factor, Boltzmann's constant, and temperature, respectively; J_{ph} is the photogenerated current density, J_s is the reverse bias saturation current density. The open-circuit voltage depends logarithmically on the short circuit density. Since short-circuit current depends linearly on light intensity, one can conclude that the open-circuit voltage also depends logarithmically on the light intensity. In Figure 3c,d, when illuminated at the same UV-C light intensity, the V_{oc} of the device with QDs fluorophor is larger than that without QDs fluorophor, indicating that higher photon current is achieved in the device with QDs, due to more down-converted photons reaching the perovskite diode. These results are good evidence that our strategy by integrating perovskite photodiode with $CsPbBr_3$ QDs fluorophor is feasible in UV-C detection. Beyond the enhanced ability for UV-C detection, our integrated perovskite photodiode array with CsPbBr3 QDs fluorophor also hold great potential applications, such as UV spectrophotometer or deep UV (DUV or UV-C) imaging.

A possible mechanism is proposed for the enhanced UV detection performance of integrated QD/perovskite photodiode and is shown in **Figure 4**. The schematic in Figure 4a illustrates the direct and indirect detection of perovskite photodiode to UV-C light. The corresponding energy diagram is present in Figure 4b. In Figure 4c, the optical transmission spectra characterizations for different substrates and films are carried out covering the full spectrum from solar blind UV wavelengths (200 nm) to visible wavelengths (900 nm). Compare to the direct detection to the UV-C light, when converted it into visible light (510 nm) by the QDs fluorophor, more converted 510 nm light could pass through the ITO/glass substrate and be absorbed by perovskite thin film due to the high transmittance of the ITO/glass substrate, leading to a high photogenerated carrier concentration, thus a large photocurrent density. Also, the UV absorption edge of our CPI film is at about 400 nm, which could effectively protect the perovskite photodiode from the degradation caused by UV light below 400 nm. When in a direct detection mode, UV light needs to go through the ITO/glass substrate before reaching the perovskite absorber layer to generate carriers. However, the UV absorption edge of our ITO/glass substrate is located at ≈300 nm, which means most of the UV light with a wavelength shorter than 300 nm is absorbed by ITO/glass substrate before they reach the perovskite diodes. In addition, though very weak UV-C light is illuminated on the perovskite layer, it may still cause a damage on the perovskite layer after a long-term exposure under UV light.

We further quantitatively evaluate the intensity of the incoming photons of UV-C light (279 nm) and the intensity of the converted visible light (510 nm) that irradiated on the perovskite absorber layer after passing through the photoconversion layer and the CPI substrate. If the light intensity of UV-C light (279 nm) source is 1 mW cm^{-2}, when downshifted into 510 nm light, the light intensity of visible light is 0.084 mW cm^{-2},

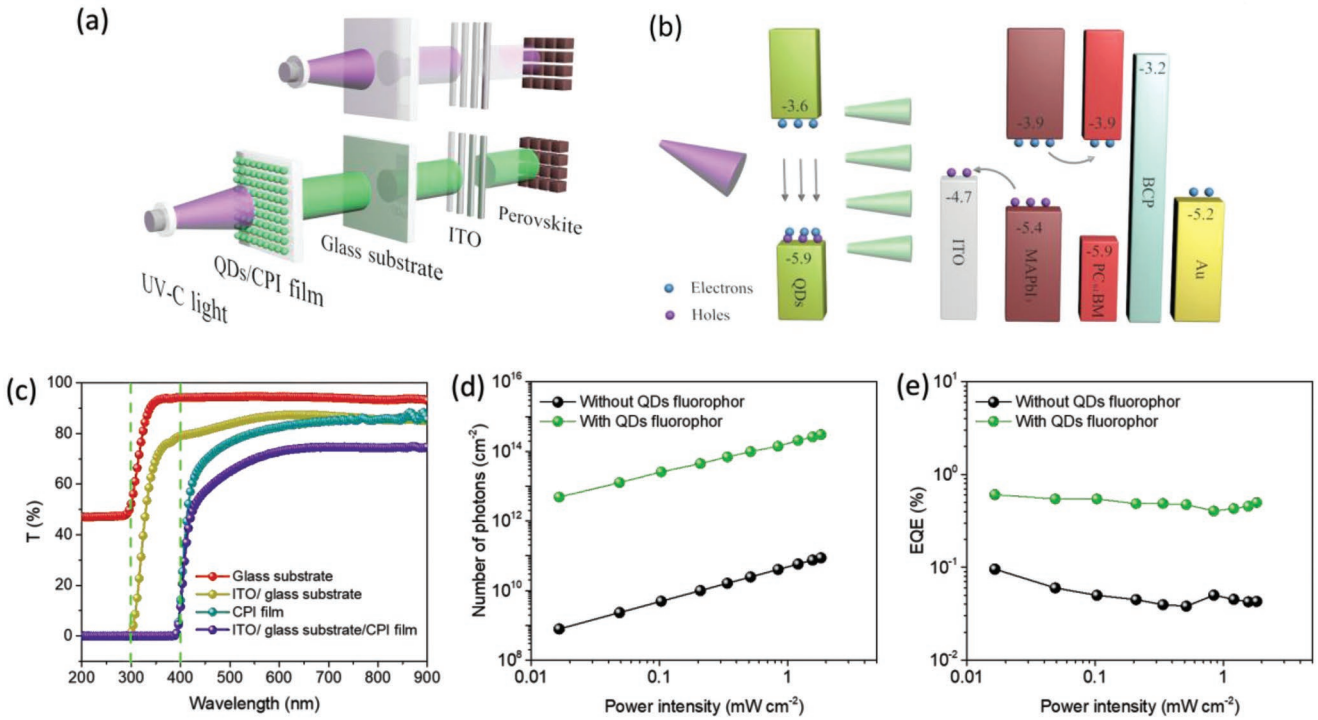

Figure 4. a) Schematic illustration of the direct and indirect detecting process of perovskite photodiode to UV-C light. b) The energy diagram of each layer. c) Optical transmission spectra of different substrates and films. d) The calculated number of photos arrived at the perovskite surface with (lower) and without down conversion by QDs fluorophor. e) EQE value of perovskite photodiode to identical incident 279 nm light intensity with or without QDs fluorophor.

since the transmittance of the ITO/glass substrate to 279 and 510 nm light is ≈0.0034% and ≈84.3% as shown in Figure 4c, therefore the light intensity that reaches perovskite diode is ≈3.4×10^{-5} mW cm^{-2} for 279 nm and 0.07 mW cm^{-2} for 510 nm. The number of photons at a certain wavelength is then calculated by using the equation[25]

$$\Phi(\text{photons/s}) = 5.03 \times 10^{12} (\text{mJ}^{-1} \times \text{nm}^{-1}) \times \lambda(\text{nm}) \times P_{\text{in}}(\text{mW}) \quad (1)$$

where P_{in} is the intensity of the monochromatic light and λ is the wavelength of the incident light. Thus, the number of photons per square centimeter can be determined corresponding to 4.8×10^{10} and 1.8×10^{14} photons cm^{-2} s for 279 and 510 nm, respectively. As a result, after the conversion of 279 nm light into 510 nm light via $CsPbBr_3$ QDs layer, the number of photons that reaches perovskite diodes significantly increase by over 3 orders of magnitude. Figure 4d shows the corresponding number of photons that reached the perovskite layer, before and after the light conversion. We also investigated the light conversion of $CsPbBr_3$ QDs fluorophor and device performance to UV-A light (369 nm) light, as shown in Figure S7 in the Supporting Information. If the light intensity of UV-A light (369 nm) source is 1 mW cm^{-2}, when downshifted into 510 nm light, the light intensity of visible light is ≈0.015 mW cm^{-2}. The transmittance of the ITO/glass substrate to 369 nm light is ≈76%. According to Equation (1), the number of photons per square centimeter that reaches perovskite diodes are calculated to be 1.4×10^{15} and 3.2×10^{13} photons cm^{-2} s for devices with and without $CsPbBr_3$ QDs, respectively. Therefore, for the UV-A region, less converted photons reach perovskite diodes, leading to a lower photocurrent, as shown in Figure S7b in the Supporting Information.

The external quantum efficiency (EQE) value can be calculated according to the equation of EQE = 1240 J_{ph}/λ P_{mono}.[25] Figure 4e shows the corresponding EQE of perovskite photodiode on the direct and indirect detection modes to UV-C light (279 nm). It is found that, when using the $CsPbBr_3$ QDs as the fluorophor, the EQE value increases from 0.045% to 0.430% when illuminated by 279 nm light with an intensity of 1.21 mW cm^{-2}. In other words, the EQE is enhanced by 10 times as shown in Figure 4e, demonstrating the superior performance of integrated QDs/perovskite photodiode.

In summary, $CsPbBr_3$ quantum dots were synthesized, which were further applied as a fluorophor in perovskite photodiode arrays for solar-blind UV light detection. By integrating as-fabricated all inorganic $CsPbBr_3$ quantum dots with hybrid organic–inorganic perovskite photodiode, the photodetection system exhibits an enhanced performance for UV-C (279 nm) light detection, with an increased responsibility and detectivity value to 1.4 mA W^{-1} and 2.4×10^{11} Jones to UV-C (279 nm) light, respectively. The improved UV-C detection performance is mainly due to the increase of the number of photons irradiated on the perovskite absorber layer by over 3 orders of magnitude via downshifting the UV-C light into visible light. On the other hand, the $CsPbBr_3$ QDs/CPI fluorophor film could effectively resist the damage of UV-C light on perovskite thin film to prolong the device lifetime. In addition, an effective approach is given in this work for the fabrication of perovskite-based photodiode array with high performance and uniformity. Our work provides a successful strategy toward high-performance perovskite-based perovskite UV-C photodetectors and promotes the development in their practical applications.

Experimental Section

Materials and Precursor Solution: PbI_2 and CH_3NH_3I (MAI) powders were purchased from Xi'an Polymer Light Technology Corp. and [6,6]-phenyl C61 butyric acid methyl ester ($PC_{60}BM$) from Luminescence Technology Corp. $PC_{61}BM$ was dissolved in 1,2-dichlorobenzene (Sigma Aldrich) with a concentration of 20 mg mL^{-1} and 2,9-dimethyl4,7-diphenyl-1,10-phenanthroline (BCP) were in isopropanol (Sigma Aldrich) for a saturated solution. The concentration for depositing MAI seed layer was 5 mg mL^{-1}, while that of MAI reaction solution was 30 mg mL^{-1} by dissolving MAI powder in isopropanol. Quantum dots solution were prepared according to the well-established method.[12b] $CsPbBr_3$ quantum dots were dispersed in hexane with the concentration of ≈ 30 mg mL^{-1}.

Device Fabrication: ITO glass substrates were subsequently cleaned by ultrasonication with deionized water, acetone, and ethanol for 10 min, respectively, and dried under nitrogen flow. Then, the substrates were treated with UV–ozone for 10 min. The MAI seed layer was spin coated on the ITO substrate at 2000 rpm for 60 s and then annealed on a hot plate at 100 °C for 10 min. After that, the powder of PbI_2 was thermally evaporated on the MAI seed layer with a pressure of ≈6×10^{-4} Pa at a deposition rate of 2–4 Å s^{-1} with a thickness of ≈150 nm using shadow mask for patterned PbI_2 thin film, while, for the control sample, the PbI_2 was directly thermally evaporated on the ITO substrate. Then, the substrates were transferred to an N_2-filled glove box and MAI solution (30 mg mL^{-1}) were spin coated on PbI_2 thin film at 2000 rpm for 60s and heated on a hot plate at 100 °C for 45 min for perovskite thin film. The unreacted MAI were washed by isopropanol solution. Subsequently, $PC_{61}BM$ and BCP were separately spin coated at 2000 rpm for 60 s. Finally, 80 nm Au contacts were deposited by thermal evaporation under high vacuum (≈5×10^{-4} Pa) with a shadow mask for patterned electrodes. For the fabrication of fluorophor film, $CsPbBr_3$ quantum dots solutions were cast on the CPI film in a glove box and annealed at 50 °C for ≈30 min. To study the influence of QDs film thickness on the light intensity of converted 510 nm light, a different amount of QDs solution was cast on a 1 cm × 1 cm CPI film. Then, these CPI films were transferred to a hot plate and annealed at 50 °C for ≈30 min. QDs/CPI film was attached with perovskite photodetector by a home-made testing fixture.

Material Characterization: Steady-state PL spectra of the $CsPbBr_3$ quantum dots on CPI film were measured by FLS920 spectrofluorometer (Edinburgh Instruments). The absolute PLQY was recorded on the Edinburgh Instruments FS5 spectrofluorometer. The UV–vis optical absorption spectra of perovskite thin films were obtained using a Shimadzu UV-2600 UV–vis spectrometer.

Device Characterization: The current density–voltage (*J–V*) characteristic behavior was measured under the dark condition and with a solar simulator (Zolix) under AM 1.5 G (100 mW cm^{-2}) by a Keithley 2400 Source in the glovebox. To investigate the photoresponse of the photodetector to monochromatic light, a laser source was used (520 nm, Shenzhen Optoelectronic Technology Co., Ltd.). In the measurement process, all devices were illuminated by light from the glass side. The light intensity was calibrated by using a power meter (Newport, 1936-R).

Supporting Information

Supporting Information is available from the Wiley Online Library or from the author.

Acknowledgements

This work is financially supported by the National Key Research and Development Program of China (2016YFA0202002),

Guangdong Natural Science Foundation (2018A030313332), and the Shenzhen Science and Technology Innovation Commission (JCYJ20160229122349365).

Conflict of Interest

The authors declare no conflict of interest.

Keywords

deep UV light, perovskite quantum dots, photodetection, photodiodes, UV-C detection

[1] a) F. Hao, C. C. Stoumpos, D. H. Cao, R. P. H. Chang, M. G. Kanatzidis, *Nat. Photonics* **2014**, *8*, 489; b) G. Xing, N. Mathews, S. Sun, S. S. Lim, Y. M. Lam, M. Gratzel, S. Mhaisalkar, T. C. Sum, *Science* **2013**, *342*, 344; c) S. D. Stranks, G. E. Eperon, G. Grancini, C. Menelaou, M. J. Alcocer, T. Leijtens, L. M. Herz, A. Petrozza, H. J. Snaith, *Science* **2013**, *342*, 341; d) J. H. Noh, S. H. Im, J. H. Heo, T. N. Mandal, S. I. Seok, *Nano Lett.* **2013**, *13*, 1764.

[2] W. Tian, H. Zhou, L. Li, *Small* **2017**, *13*, 1702107.

[3] a) B. R. Sutherland, A. K. Johnston, A. H. Ip, J. Xu, V. Adinolfi, P. Kanjanaboos, E. H. Sargent, *ACS Photonics* **2015**, *2*, 1117; b) Y. Fang, J. Huang, *Adv. Mater.* **2015**, *27*, 2804; c) J. Zhou, J. Huang, *Adv. Sci.* **2018**, *5*, 1700256.

[4] a) S. Yakunin, M. Sytnyk, D. Kriegner, S. Shrestha, M. Richter, G. J. Matt, H. Azimi, C. J. Brabec, J. Stangl, M. V. Kovalenko, W. Heiss, *Nat. Photonics* **2015**, *9*, 444; b) S. Yakunin, D. N. Dirin, Y. Shynkarenko, V. Morad, I. Cherniukh, O. Nazarenko, D. Kreil, T. Nauser, M. V. Kovalenko, *Nat. Photonics* **2016**, *10*, 585; c) H. Wei, Y. Fang, P. Mulligan, W. Chuirazzi, H.-H. Fang, C. Wang, B. R. Ecker, Y. Gao, M. A. Loi, L. Cao, J. Huang, *Nat. Photonics* **2016**, *10*, 333.

[5] a) G. Maculan, A. D. Sheikh, A. L. Abdelhady, M. I. Saidaminov, M. A. Haque, B. Murali, E. Alarousu, O. F. Mohammed, T. Wu, O. M. Bakr, *J. Phys. Chem. Lett.* **2015**, *6*, 3781; b) E. Zheng, B. Yuh, G. A. Tosado, Q. Yu, *J. Mater. Chem. C* **2017**, *5*, 3796; c) X. Hu, X. Zhang, L. Liang, J. Bao, S. Li, W. Yang, Y. Xie, *Adv. Funct. Mater.* **2014**, *24*, 7373; d) Y. Guo, C. Liu, H. Tanaka, E. Nakamura, *J. Phys. Chem. Lett.* **2015**, *6*, 535; e) V. Adinolfi, O. Ouellette, M. I. Saidaminov, G. Walters, A. L. Abdelhady, O. M. Bakr, E. H. Sargent, *Adv. Mater.* **2016**, *28*, 7264.

[6] X. Xu, C.-C. Chueh, P. Jing, Z. Yang, X. Shi, T. Zhao, L. Y. Lin, A. K. Y. Jen, *Adv. Funct. Mater.* **2017**, *27*, 1701053.

[7] a) H. Chen, K. Liu, L. Hu, A. A. Al-Ghamdi, X. Fang, *Mater. Today* **2015**, *18*, 493; b) L. Sang, M. Liao, M. Sumiya, *Sensors* **2013**, *13*, 10482; c) E. Monroy, F. Omnès, F. Calle, *Semicond. Sci. Technol.* **2003**, *18*, R33.

[8] H. Zhou, Z. Song, P. Tao, H. Lei, P. Gui, J. Mei, H. Wang, G. Fang, *RSC Adv.* **2016**, *6*, 6205.

[9] P. Michaloski, P. Dewa, *SPIE* **1988**, *998*, 38.

[10] S. Tandon, S. Ghosh, J. Hutchings, C. Stalin, A. Subramaniam, *Curr. Sci.* **2017**, *113*, 583.

[11] a) X. Li, J. Yang, Q. Jiang, H. Lai, S. Li, J. Xin, W. Chu, J. Hou, *ACS Nano* **2018**, *12*, 5605; b) F. Bella, G. Griffini, J. P. Correa-Baena, G. Saracco, M. Gratzel, A. Hagfeldt, S. Turri, C. Gerbaldi, *Science* **2016**, *354*, 203.

[12] a) Y. Wang, X. Li, J. D. Song, L. Xiao, H. Zeng, H. Sun, *Adv. Mater.* **2015**, *27*, 7101; b) L. Protesescu, S. Yakunin, M. I. Bodnarchuk, F. Krieg, R. Caputo, C. H. Hendon, R. X. Yang, A. Walsh, M. V. Kovalenko, *Nano Lett.* **2015**, *15*, 3692; c) Q. Chen, J. Wu, X. Ou, B. Huang, J. Almutlaq, A. A. Zhumekenov, X. Guan, S. Han, L. Liang, Z. Yi, J. Li, X. Xie, Y. Wang, Y. Li, D. Fan, D. B. L. Teh, A. H. All, O. F. Mohammed, O. M. Bakr, T. Wu, M. Bettinelli, H. Yang, W. Huang, X. Liu, *Nature* **2018**, *561*, 88; d) K. Lin, J. Xing, L. N. Quan, F. P. G. de Arquer, X. Gong, J. Lu, L. Xie, W. Zhao, D. Zhang, C. Yan, W. Li, X. Liu, Y. Lu, J. Kirman, E. H. Sargent, Q. Xiong, Z. Wei, *Nature* **2018**, *562*, 245; e) N. Wang, W. Liu, Q. Zhang, *Small Methods* **2018**, *2*, 1700380.

[13] W. Chen, Y. Liu, Z. Yuan, Z. Xu, Z. Zhang, K. Liu, Z. Jin, X. Tang, *J. Radioanal. Nucl. Chem.* **2017**, *314*, 2327.

[14] J. Lu, X. Sheng, G. Tong, Z. Yu, X. Sun, L. Yu, X. Xu, J. Wang, J. Xu, Y. Shi, K. Chen, *Adv. Mater.* **2017**, *29*, 1700400.

[15] M. Zhang, L. Wang, L. Meng, X.-G. Wu, Q. Tan, Y. Chen, W. Liang, F. Jiang, Y. Cai, H. Zhong, *Adv. Opt. Mater.* **2018**, *6*, 1800077.

[16] S. Sun, D. Yuan, Y. Xu, A. Wang, Z. Deng, *ACS Nano* **2016**, *10*, 3648.

[17] H. Wei, X. Zhao, Y. Wei, H. Ma, D. Li, G. Chen, H. Lin, S. Fan, K. Jiang, *NPG Asia Mater.* **2017**, *9*, e395.

[18] W. Lee, J. Lee, H. Yun, J. Kim, J. Park, C. Choi, D. C. Kim, H. Seo, H. Lee, J. W. Yu, W. B. Lee, D. H. Kim, *Adv. Mater.* **2017**, *29*, 1702902.

[19] L. Gu, M. M. Tavakoli, D. Zhang, Q. Zhang, A. Waleed, Y. Xiao, K. H. Tsui, Y. Lin, L. Liao, J. Wang, Z. Fan, *Adv. Mater.* **2016**, *28*, 9713.

[20] L. Dou, Y. M. Yang, J. You, Z. Hong, W. H. Chang, G. Li, Y. Yang, *Nat. Commun.* **2014**, *5*, 5404.

[21] C. Bao, Z. Chen, Y. Fang, H. Wei, Y. Deng, X. Xiao, L. Li, J. Huang, *Adv. Mater.* **2017**, *29*, 1703209.

[22] X. Gong, M. Tong, Y. Xia, W. Cai, J. S. Moon, Y. Cao, G. Yu, C.-L. Shieh, B. Nilsson, A. J. Heeger, *Science* **2009**, *325*, 1665.

[23] a) Y. Liu, Y. Zhang, K. Zhao, Z. Yang, J. Feng, X. Zhang, K. Wang, L. Meng, H. Ye, M. Liu, S. Liu, *Adv. Mater.* **2018**, *30*, 1707314; b) R. Nasanen, H. Ojanpaa, T. Tanskanen, J. Paallysaho, *Exp. Brain Res.* **2006**, *172*, 464.

[24] G. A. H. Wetzelaer, M. Kuik, M. Lenes, P. W. M. Blom, *Appl. Phys. Lett.* **2011**, *99*, 153506.

[25] Z. Chen, T. G. Deutsch, H. N. Dinh, K. Domen, K. Emery, A. J. Forman, N. Gaillard, R. Garland, C. Heske, T. F. Jaramillo, A. Kleiman-Shwarsctein, E. Miller, K. Takanabe, J. Turner, *Photoelectrochemical Water Splitting: Standards, Experimental Methods, and Protocols*, Springer, New York **2013**, p. 87.